Measuring blood vessel sizes using simultaneous gradient- and spin-echo acquisition at 7T MRI

Mar Fernandez Salamanca, Physics Department, Utrecht University.

First advisor: Jeroen Siero, Beeld Divisie, UMC, Utrecht.

Second advidsor: Mario Baez Yanez, Beeld Divisie, UMC, Utrecht.

(Dated: February 3, 2020)

The research work described in this thesis focuses on vessel size imaging. The method explained in the project can be used for a better understanding of tumor characterization, the growth of new vessels or micro-vessel revascularization. To begin with, a deep understanding of the physics behind this phenomenon is explained. Moreover, the behaviour of the transverse relaxation rates ΔR_2 (Spin echo sequence) and ΔR_2^* (Gradient echo sequence) in presence of microspheres is analyzed. More specifically, the dependence of the ΔR_2^* in terms of the diameter of the spheres is calculated experimentally. This is accomplished by studying the nature of these transverse relaxation rates and its dependencies on different parameters such as main magnetic field, pulse sequence, magnetic susceptibility among others. Different phantom experiments have been employed, showing inconsistent results regarding the theory. Finally, possible solutions to this evidences are introduced.

Keywords: 7T MRI, transverse relaxation rates, diffusion, magnetic susceptibility, vessel size imaging, static dephasing regime, narrowing diffusion regime.

I. INTRODUCTION:

A higher resolution MRI generation is becoming an useful tool for the study of the brain microvasculature architecture, helping to better understand brain tumors [1] (before and after radiotherapy), strokes [2] and even Alzheimer [3] . Nowadays, in order to get a resolution of the order of micrometers, higher field MRI is performed. Stronger magnets with a main magnetic field (B_0) larger than 7T are used. These induce a signal proportional to B_0^2, hence the signal-to-noise ratio (SNR) which relates the signal amplitude with the standard deviation of noise is also increased [4]. This means that in comparison with lower magnetic field scanners, the signal obtained from a 7T scanner is increased while the noise is kept constant, thus the SNR is also increased (SNR$\propto B_0$). This increment in SNR allows a higher spatial resolution by maintaining the noise relatively low.

The measured MRI signal is related to the dissipation process of the body water protons after an excitation pulse (B_1) has been applied. This nuclear phenomenon is characterized by the longitudinal (T_1) and transverse (T_2) times [5] or, the also used relaxation rates, which are the inverse function of the relaxation times ($R_i = 1/T_i$ with $i = 1, 2$). In particular, since the measured MRI signal decay is given by the transverse component of the magnetic field, T_2 (or R_2) is the relaxation time of interest. More specifically, the signal decay is exponentially associated with the relaxation rates as $S \propto \exp^{-R_2 \cdot t}$. However, depending on the sequence used in the scan, there can be an extra contribution due to field inhomogeneities across a voxel ($R_{2'} = 1/T_{2'}$). Then, the effective relaxation rate becomes $R_{2*} = R_2 + R_{2'}$ (or $1/T_{2*} = 1/T_2 + 1/T_{2'}$). However, these relaxation rates depend on some factors as changes in magnetic susceptibility or diffusion among others. Firstly, changes in magnetic susceptibility due to a variation of oxygenation in blood or to the presence of a paramagnetic contrast agent lead to a ΔR_2^* and ΔR_2. Ones of the most used paramagnetic contrast agents in MRI are Gadolinium-DTPA (Gd-DTPA) and Dysprosium-DTPA (Dy-DTPA). Both can be used, for instance, to reduce blood T_1 and T_2 and water contrast thanks to its magnetic nature. Secondly, diffusion of water molecules attend to a irreversible loss of phase coherence costing signal intensity in spin echo (SE) sequences. Thirdly, magnetic field perturbations create a reversible heterogeneity of phase distribution. This causes a decrease of signal in gradient echo (GRE) sequences, therefore an increase on ΔR_2^*. All previous conditions are explained in detail by Tropès et al [6]. Finally, both ΔR_2^* and ΔR_2 are directly dependent on the size and geometry of the studied vasculature. Especially, this vessel size dependence is the main key to this project. In this project, a relation between the vessel size and the changes in the relaxation rates is explored. These results are achieved in a 7T Philips MRI machine using a phantom with different sizes of glass/polystyrene microspheres that mimic the brain vessels.

Approximately two decades ago Monte Carlo simulations and experiments in rats were performed to obtain and understand better this size dependence of ΔR_2^* and ΔR_2 at $1.5T$ MRI [7, 8]. The relation obtained for both GRE and SE sequences is shown in Fig1.

The peak in relaxation time for the SE sequence is obtained around $r = 5\mu m$. It also matches to the relaxation time value where the GRE sequences reaches a plateau. The GRE values are always bigger than SE values.

Nevertheless, higher field MRI machines have become available. In the first part of this project a Philips $7T$ MRI machine is used to obtain both ΔR_2^* and ΔR_2 vessel size dependence by using a simultaneous SE/GRE acquisition sequence. A few years ago, Tropès et al [9] performed a simulation that, together with the high field MRI theory, shows the size dependence for differ-

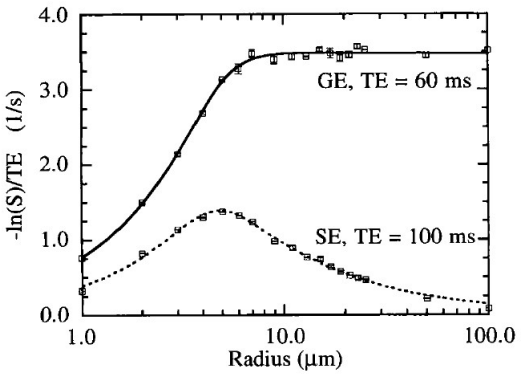

Figure 1: Size dependence of ΔR_2^* $(GRE, TE = 60ms)$ and ΔR_2 $(SE, TE = 100ms)$ for $\Delta\chi = 1 \times 10^{-7}$ and a 2% volume fraction by using magnetized cylinders for the simulation [8].

ent B_0 fields, including $B_0 = 7T$. In order to experimentally achieve this dependence, a phantom is built (see Appendix A for more information about the phantom structure). A range of different sizes of microspheres are placed inside this phantom representing the different brain vessels that actually want to be studied in *in vivo* patients. In order to carry out this experiment a series of assumptions related to the phantom are taken into account based on Yablonskiy's and Haacke's work [10]:

- A **Static dephasing regime** is assumed where the diffusion length of water molecules (L_D) is supposed to be much shorter than the microsphere's radius. Then, the signal decay can be assumed as monoexponential, $S \propto e^{-R_2 t}$ for SE or $S \propto e^{-R_2^* t}$ for GRE.
- A **statistical approach** is presumed where the microspheres are randomly distributed in the medium and the average number of microspheres in the volume of interest is much bigger than 1.
- The **low concentration limit**. The relative volume fraction $\varrho = v/V$, where $v \equiv$net volume of the microspheres and $V \equiv$ net volume of the microspheres plus the solution, must satisfy that $\varrho << 1$. This is related to no signal been considered coming from the inside of the microspheres.

The principal advantages of increasing the main magnetic field are increasing the SNR and reducing to lower perturber's sizes the Static dephasing regime condition.

Finally, after performing a SE/GRE simultaneous sequence and by applying image processing, a ΔR_2^* and ΔR_2 vessel size dependence is obtained.

This results could be used to evaluate the repercussion of cancer therapy or the better understanding of pre, during and post stroke illness for example. Moreover, it can help with tumor characterization and with the growth of new vessels. Furthermore, it will be useful in visualization of spheres that provide radionuclide delivery to liver tumors for example. Besides, vessel size imaging in healthy brains can provide an extra knowledge to fMRI analysis. In conclusion, the applications of this method can be useful for a large variety of fields that involve micro vasculature imaging.

II. THEORY

In this section physical concepts in relation with MRI and this experiment are explained. First of all, a brief explanation on magnetism is done. After that, the physical phenomenon of MRI is explained, called NMR, followed by an explanation of a basic NMR procedure. It consists of applying a Radio-Frequency pulse that will tip the magnetization created by the protons a certain angle creating two components, a transverse magnetization M_{xy} and a longitudinal magnetization M_z. Then, the behaviour and meaning of each magnetization component will be explain in order to obtain a NMR signal. Subsequently, two of the basic pulse sequences in MRI ,Spin echo (SE) and Gradient echo (GRE), are explained. Moreover, two regimes in terms of signal decaying, Static Dephasing Regime and Narrowing Diffusion Regime, are considered. To end, relaxation rates dependencies are explained to understand how they react to changing certain parameters.

A. Magnetism, magnetic dipole moments and Magnetic Susceptibility

One of the essential properties of matter for MRI is magnetism. That property is based on the fact that the movement of charges produce magnetic forces, thus the magnetism is a consequence of electricity and movement. The smallest natural magnet is the electron that inside of an atom is on the move and it has a charge, creating a minuscule magnetic field. Then, the magnetic properties of the materials result from the orientation and configuration of the electrons that form theirs atoms. In some materials, the electrons form domains (regions inside an atom where the electrons have the same orientation). If these electrons are orientated randomly, non magnetic properties arises from them. On the other hand, the materials that have the individual domains aligned in one direction thus exhibit magnetic properties are called permanent magnets [4]. This behaviour is a microscopic effect created by the electrons in movement.

Moreover, a charged particle with sphere geometry in rotation also creates a magnetic dipole moment $\boldsymbol{\mu}$ (with magnitude μ and a direction). Now, the effect is macroscopic and produced by particles with a certain geometry and rotation.

On the previous figure (Fig2), the field produced by

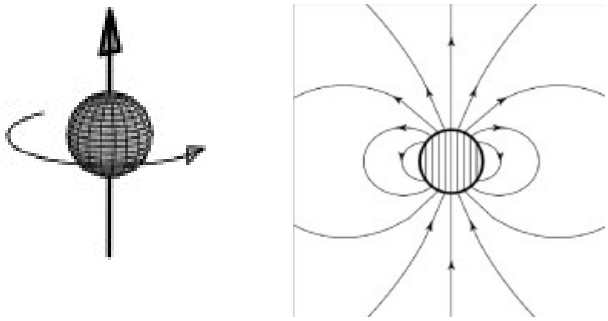

Figure 2: (a)Spinning charged sphere rotating around the z-axis creates a magnetic dipole moment on the spin axis of the sphere. (b)Magnetic dipole field lines (B_z) outside produced by the sphere dipole moment. Image obtained from [11]

a magnetic dipole is shown. Knowing that the dipole moment is proportional to the volume of the sphere, the charge (Q) and the angular frequency (ω), the z-component of the field is given by the following equation:

$$B_z = \frac{\mu(3cos^2(\theta) - 1)}{r^3} \tag{1}$$

where r is the radius of the sphere, μ is the magnitude of the dipole moment and θ is the angle between the dipole moment vector and the magnetic field [11]. In (Fig2), the angle would be $\theta = 0$ because both vectors are in the z-direction. A contour map (Fig3) of this z-component is of big importance since this will be the component adding tho the external applied magnetic field B_0 in order to create field distortions.

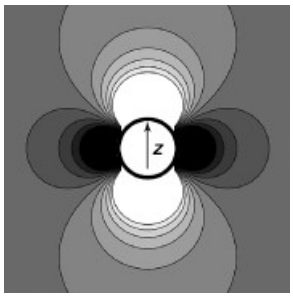

Figure 3: Contours of equal B_z. Figure obtained from [11].

Then, we need to discuss what happens when this dipole is placed in an external magnetic field $\boldsymbol{B}$. First of all, due to the orientation dependence of the dipole moment, the $\boldsymbol{B}$ creates a torque $\boldsymbol{W}$ (Eq2) on the dipole that would favor to align with $\boldsymbol{B}$ when $\boldsymbol{\mu}$ is initially at an angle to the magnetic field.

$$\boldsymbol{W} = \boldsymbol{\mu} \times \boldsymbol{B} = \mu B sin(\theta) \tag{2}$$

Secondly, if this magnetic field is homogeneous no net force will exist. Otherwise, if $\boldsymbol{W} \equiv \boldsymbol{B(z)}$ depends on the position, a net force $\boldsymbol{F}$ (Eq3) will pull the dipole towards a stronger field region.

$$F = \mu \frac{dB}{dz} \tag{3}$$

Lastly, but no less important, the energy of the dipole. This energy is given by the following equation:

$$E = -\boldsymbol{\mu} \cdot \boldsymbol{B} = -\mu B cos(\theta) \tag{4}$$

where θ is the angle that forms $\boldsymbol{B}$ and $\boldsymbol{\mu}$ that shows the orientation dependence of the dipole energy. The lowest energy is then achieved when both vectors are aligned ($\theta = 0$) [11]. But differences on orientation cause unbalanced forces that creates a torque. Moreover, in the case where the external magnetic field is not uniform, this torque is not created because of the orientation difference but for the curving field lines. In both cases, where the torque is created, a net force appears towards the region of stronger field.

Another important characteristic of materials for MRI is the magnetic susceptibility. The magnetic susceptibility is the capability of a material to become magnetized when is placed in a magnetic field B_0. Then, by placing an object inside a magnetic field B_0, local induced magnetization variations are created around the object. This local magnetic field becomes $B_0 + \Delta B$, where the ΔB is the object's induced internal field contribution. This induced internal magnetization can oppose or go in the same direction that the B_0 field [11]. In the first case the local magnetic field surrounding the object is lowered and in the second case is increased. Materials are classified in three groups depending on their magnetic behaviour:

- **Paramagnetic** These materials are attracted by a magnet. They increase the local magnetic field while aligning as B_0 and they have a slightly positive magnetic susceptibility (Fig4 left side). Examples are Dysprosium or Gadolinium based contrast agents and deoxyhemoglobin.

- **Ferromagnetic** These elements are strongly attracted towards a magnet. They are also called "superparamagnetic" materials. Moreover, they aligned in the same direction as the external magnetic field B_0, increasing the local magnetic field in the region surrounding the object. Examples are iron, magnetite and nickel.

- **Diamagnetic** These materials are repelled by a magnet. When an external magnetic field is applied, they oppose it and decrease the local magnetic field around them (Fig4 right side). Moreover they have a negative magnetic susceptibility. Examples are calcium, hemoglobin and water.

B. Nuclear Magnetic Resonance (NMR)

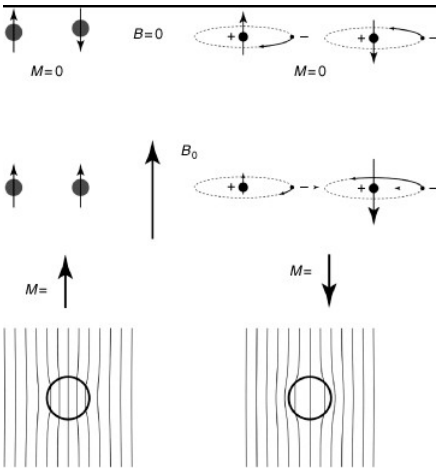

Figure 4: Paramagnetic behaviour on the left side and diamagnetic on the right of the image. Image obtained from [11].

Nuclear Magnetic Resonance is the basis of MRI. Its work is to study the magnetic properties of the nucleus of the atoms. Our body consists is formed mainly of water H_2O, so a large amount of Hydrogen atom are contented in it. The magnetic behaviour of these hydrogen atoms (composed by one proton in the nucleus) can be explained with the rotating sphere model explained in the previous subsection II A.

Firstly, two physical phenomena that are of high importance in order to understand NMR are explained: Relaxation and Precession of the nucleus. Secondly, a NMR basic procedure is shown.

1. Relaxation

The relaxation property of the nucleus come from the fact the any thermodynamic system tends to equilibrium. Energetically, in all cases, the effect of an external magnetic field is to drive all the nucleus towards the lowest energy level. Thermodynamically, any system is constantly exchanging energy between its different modes (rotational, vibrational and traslational). Then, by increasing the temperature, the energy in all three modes increases as well, thus alignment of the nucleus becomes harder to obtain. Then, the equilibrium state (lowest energy state of the system) is easier to achieve when the temperature is low. Mathematically, this phenomena can be understood by supposing a two states level problem. The positive state (+) corresponds to the spins aligned parallel with the external magnetic field B_0 and the negative state (-) corresponds to the spins opposed to B_0. Then, the population ratio between these two states at thermal equilibrium can be explained thanks to the Maxwell-Boltzmann statistics by the following equation [11]:

$$\frac{n_+}{n_-} = e^{-\Delta E/k_B T} \tag{5}$$

where $k_B = 1.38\times10^{-23}$ $[J/K]$ is the Boltzmann's constant, T is the temperature and ΔE is the energy difference between the two states given by $\Delta E = -2\mu B_0$ (with a negative signed because $E_- > E_+$). This ratio between population is usually really small (10^{-5} at room temperature in a 1.5T field), but it creates a small equilibrium magnetization M_0. By lowering the temperatures, the ratio also decreases, and for high temperatures this ratio approaches 1. Since $\Delta E/k_b T \ll 1$ we can Taylor expand the exponential and obtain

$$M_0 \approx \frac{n\mu^2 B_0}{k_B T} \tag{6}$$

where $n = n_+ + n_-$ is the total spin density. So, the equilibrium magnetization is proportional to the applied magnetic field and the spin density and inversely proportional to the temperature. Moreover, without going into further details, the precession of this magnetization during resonance will create an small electrical current in the receiver coil known as MR signal.

2. Precession

Now, the second effect which gives meaning to NMR is the precession of the nucleus. This physical behaviour is due to the fact that nucleus also possess angular momentum [11]. Since both moments, dipole moment ($\boldsymbol{\mu}$) and angular moment ($\boldsymbol{L}$), are related to how fast the proton is spinning, thus a proportionality constant is defined:

$$\gamma = \frac{\mu}{L} \tag{7}$$

This constant is called "gyromagnetic ratio" and is particular for each element. Some examples can be seen in the following table:

Nucleus	^1H	^{13}C	^{17}O	e
$\boldsymbol{\gamma/2\pi}$ [MHz/T]	42.58	10.7	−5.8	28024

Table I: Gyromagnetic value for various elements.The elements with negative values precess counterclockwise and the ones with positive values precess clockwise. Table obtained from [12].

From Table I we can see that the elements with a higher mass have the lower gyromagnetic ratio values. This is because the dipole moment is proportional to Q/m (where Q is the charge and m is the mass), thus $\gamma \propto 1/m$.

On the previous section II A, the torque was expressed as the magnetic torque on the dipole moment. In this

case, it is expressed as the rate of change of the spin angular momentum.

$$\boldsymbol{W} = \frac{d\boldsymbol{L}}{dt} = \gamma \boldsymbol{L} \times \boldsymbol{B_0} \tag{8}$$

Then, precession emerges because the $d\boldsymbol{L}/dt$ and $\boldsymbol{L}$ always form a 90 degree angle.

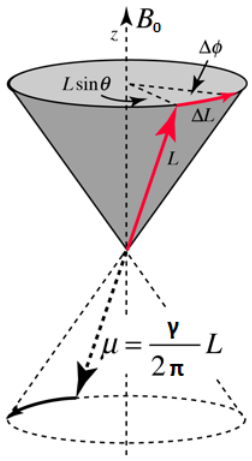

Figure 5: The spin precesses around the B_0 without changing the angle (θ) that it makes with the field. The angular momentum is increased by ΔL but it never changes its magnitude, it is just a rotation. Image from [12].

Actually, the most important characteristic of the precession movement is the frequency at which the spin precesses. This frequency is an essential factor for NMR, thus MRI. In a time interval dt, the precession angle is defined by $\Delta\phi = \Delta\boldsymbol{L}/\boldsymbol{L} = \gamma B_0 dt = \omega_0 dt$. This ω_0 frequency is known as the Larmor frequency and is the key for MRI. These two processes, relaxation and precession, are the basics of NMR. Over time, relaxation drives to a gradual alignment with the magnetic field while precession does not interfere. Moreover, the time scale of both processes are orders of magnitude distant. At 1.5T, the precession period ($1/\omega_0$) is about $10^{-8}s$ whereas the relaxation time (T_1) needed to reach the thermal equilibrium (Fig8B) is about $1s$ [11].

3. Radio-Frequency pulse, Magnetization components and Relaxation times

When the main magnetic field is applied, the nucleus tend to aligned parallel or anti-parallel with it, thus the magnetization vector of the nucleus ($\boldsymbol{M}$) with maximum magnitude M_0 points in the same direction or opposed to $\boldsymbol{B_0}$. During a few milliseconds an oscillating current is applied to the transmitted coil that produces an oscillating magnetic field ($\boldsymbol{B_1}$) that fluctuates in the radio-frequency regime. This is what we know as Radio-Frequency (RF) pulse or B_1 field and it is in charge of tipping the spins a certain angle away from $\boldsymbol{B_0}$. This magnetic field is orders of magnitude smaller than the main magnetic field. For example, in a 1.5T scanner the RF pulse oscillates at a frequency of $64MHz$ that correspond to a magnetic field magnitude of a few microteslas. Moreover, not all the RF pulses will create a signal to detect. A nucleus is able to absorb electromagnetic energy from the RF pulse when both oscillates at the same frequency. So, $\boldsymbol{B_1}$ needs to oscillate at a frequency equal to the Larmor frequency of the spin to create a resonance phenomenon, hence a weak and transient detectable signal [4]. Then, as the name Magnetic Resonance Imaging implies, the signal comes from a resonance effect between the frequency at which the nucleus are precessing and the frequency of the RF pulse. Finally, all the while the RF pulse is turned on and the magnetization vector is slightly tipped, $\boldsymbol{M}$ starts to precess around and further away of the $\boldsymbol{B_0}$ field, tracing out a spiral as we can see in the following figure:

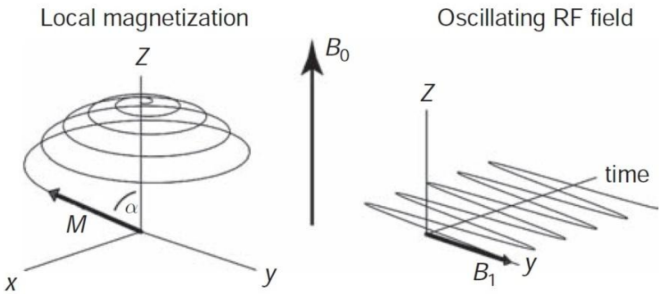

Figure 6: Tipping the magnetization $\boldsymbol{M}$ with an oscillating RF pulse, in this case perpendicular to $\boldsymbol{B_0}$(right figure). The magnetization vector starts to precess and falling away of the main magnetic field due to this pulse. The maximum angle α that $\boldsymbol{M}$ forms with $\boldsymbol{B_0}$ is called the flip angle. Figure from [11].

So, the angle between $\boldsymbol{M}$ and $\boldsymbol{B_0}$ is known as the Flip angle (α). This flip angle (9) can be modified by adjusting the time duration of the pulse.

$$\alpha = \frac{\gamma}{2\pi} B_1 dt \tag{9}$$

Furthermore, this magnetization precession generates a magnetic field variable in time that induces a current in the receiving coil. This induced current creates a measurable signal which is proportional to the magnitude of the precessing magnetization and is called Free Induction Decay (FID) signal. These three words have a naturally purpose:

- *Free* comes from the fact that the spins precess freely.
- *Induction* is related with the current induced by a changing magnetic field.

- *Decay* describes the transient behaviour of the signal.

So, the new characteristic appears with the word "*Decay*". The signal is reduced in time because the nucleus are dephasing, thus they are loosing phase coherence. Each spin senses a different and random fluctuating field that adds to B_0. These differences in magnetic field are the reason that the spins precess at a different rate, so as time goes on the spins are more out of phase with one another and they do not add coherently anymore. This loss in coherence causes the exponential decay of the FID signal. The decay constant T_2 is called transverse relaxation.

In summary, when a sample is placed inside a magnetic field B_0, the nucleus tend to align parallel or antiparallel to it depending of their magnetic properties. Due to this alignment of the spins a maximum magnetization is formed because of the relaxation property of the spins. This maximum value of the magnetization is called equilibrium magnetization M_0 (see Fig7A). Then, a RF pulse, with a frequency equal to the Larmor frequency, is applied tipping the magnetization at an angle α known as the flip angle (see Fig7B). Then, the magnetization vector can be decomposed into two magnetization components, a longitudinal magnetization M_L (parallel to B_0) and a transverse magnetization M_T (perpendicular to B_0). The signal created is only coming from the transverse magnetic component $S \propto M_T$, since is the one inducing an oscillating current in the receiver coil of the scanner that can be detected (see Fig7C). Since every spin feels a different pattern of fluctuating magnetic fields, they start to precess in a different rate creating phase dispersion. In other words, they start to dephase, thus the system losses coherence and the signal. This M_T decay can be assumed as exponential with a decay constant of $1/T_2$ or $1/T_2^*$ depending of the used pulse sequence (see Fig 8a). Meanwhile, the entire system is addressed to equilibrium (lowest energy level of the system), so M_L regrows as $M_L = M_0(1 - e^{-t/T_1})$ where T_1 is the longitudinal relaxation time constant (see Fig8b).

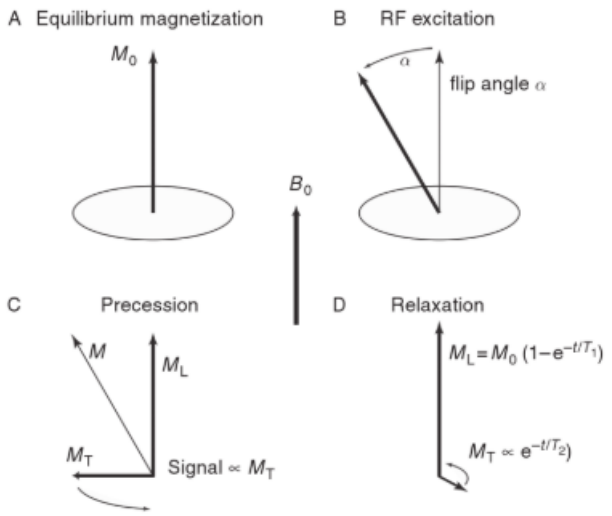

Figure 7: A. Equilibrium magnetization aligned with the B_0 field. B. RF pulse applied, thus the magnetization vector is tipped a certain flip angle. C. Magnetization vector starts to precess around B_0. D. Regrowth of the longitudinal component to reach the equilibrium magnetization again and decay of the transverse component due to the loss of coherence. Figure from [11].

C. Pulse sequences: Spin Echo and Gradient Echo

Two of the basic pulse sequences in MRI are Spin echo (SE) and Gradient echo (GRE). Both sequences have a similar structure, first a pulse is applied and after a fixed time, called Echo time (TE), a signal is received.

1. Spin echo

When the B_0 of the MRI machine is activated all the spins aligned in a parallel or anti-parallel way (depending on the magnetic behaviour of the sample). Then, an excitation pulse is applied (Radio-Frequency pulse). This pulse is usually of 90 degrees, but the actual value will depend on the purpose of the scan. This pulse generates a Free Induction decay (FID) that decays away quickly because of T_2^* which is related to magnetic field inhomogeneities. All the nucleus are in the transverse magnetization plane and they start to precess at different rates due to field inhomogeneities. At a time equal to half the echo time a rephasing pulse (180 degrees) is applied to reverse the sign of the phase of each spin. Finally, at the echo time all the spins are in phase again and add coherently to give a signal. This rephasing pulse recovers for the dephasing caused by the field inhomogeneities, thus the final signal intensity is given by a T_2 decay (Fig 9). This procedure is repeated after each Repetition time (TR).

2. Gradient echo

In this case, instead of using a 180 degree pulse to induce the echo, magnetic field gradients are used. The excitation pulse is applied and the nucleus are sent to the transverse plane as in a SE sequence. An instant later a gradient is applied to accelerate the dephasing phenomenon. At halved the echo time this gradient is instantly reversed (inversion of polarity), thus the spins starts to rephase. The echo is obtained once the rephasing gradient has been turn on the same amount of time as the initial gradient. In this case the signal decay is given by T_2^* (Fig 10) since the rephasing gradient only recovers for the dephasing caused by the first gradient.

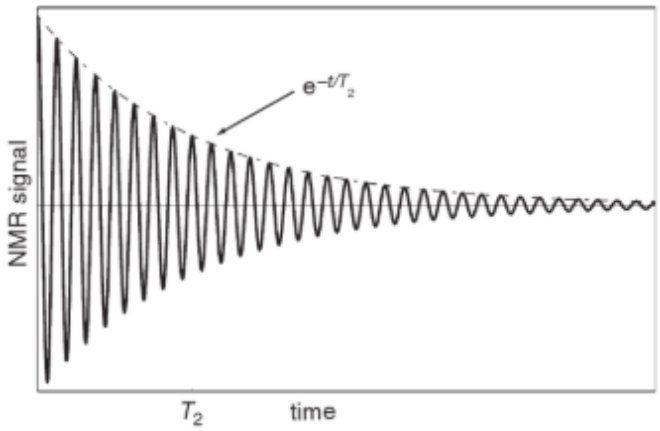

(a) Free induction decay signal ruled by T_2 transverse relaxation time constant. Image from [12].

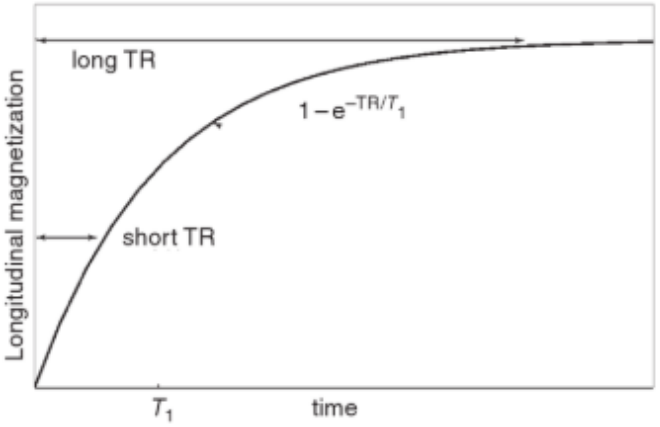

(b) Regrowth of the longitudinal magnetization ruled by T_1 to reach the equilibrium state. Image from [12].

Figure 8: T1 and T2 description.

So, this sequence is sensitive to field inhomogeneities.

To sum up, in Spin Echo, the inhomogeneities from the B_0 and the ones created by the tissue susceptibilities are corrected by the rephasing RF pulse. On the other hand, in a Gradient Echo sequence, the dephasing/rephasing gradients occur in the same direction as the B_0 field, thus not cancelling the inhomogeneities effects. In other words, the rephasing gradient only corrects for the dephasing created by the first applied gradient. So, a Spin echo sequence emphasize a T_2 decay while a Gradient echo sequence emphasize a T_2^* decay.

D. Static Dephasing regime vs Narrowing Diffusion regime

Until know, the mono-exponential decay behaviour assumed for the signal comes from eliminating the diffusion contribution in the Bloch-Torrey equation (Equation 10).

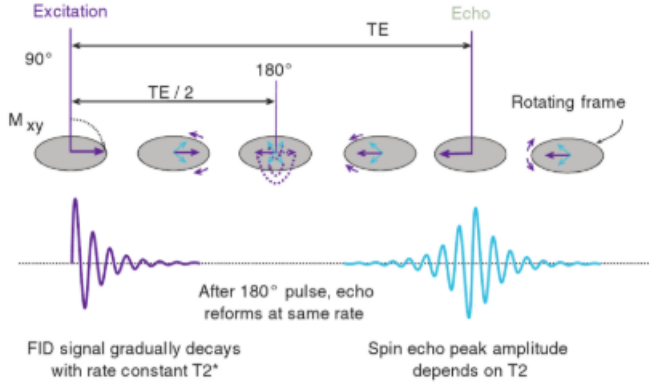

Figure 9: Spin echo sequence. At $t = 0$ a 90 degree pulse is applied and all the spins are sent to the transverse plane. They start to dephase since they are precessing at different rates due to field inhomogeneities (FID due to T_2^*). At $t = TE/2$ a 180 degree pulse is applied and the transverse plane is flipped as a *pancake*, thus the phases are inverted. Finally, at $t = TE$ all the spins are in phase again and they add coherently giving a measurable signal. Image from [12], Figure 14-17.

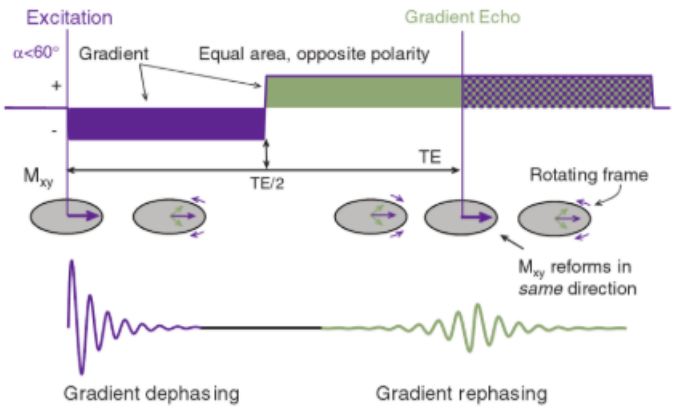

Figure 10: Gradient echo sequence. At $t = 0$ an excitation pulse is applied. After it, a gradient is turned on during a period of time equal to $TE/2$. The spins start to dephase due to the gradient and the field inhomogeneities. At $t = TE/2$ this gradient is reversed in polarity and the spins start to rephase creating an echo at $t = TE$. Image from [12], Figure 14-29.

$$\frac{d\boldsymbol{M}}{dt} = \gamma(\boldsymbol{M}x\boldsymbol{B_0}) + \begin{pmatrix} \frac{M_x}{T_2} \\ \frac{M_y}{T_2} \\ \frac{M_0 - M_z}{T_1} \end{pmatrix} + D\nabla^2\boldsymbol{M} \qquad (10)$$

So, if diffusion becomes significant, the signal is no longer decaying mono-exponentially. Then, all the theory regarding signal decay explained above is not entirely true anymore since an extra contribution due to diffusion needs to be taken into account. Moreover, solving

the Bloch-Torrey equation with the diffusion contribution can no longer be done analytically. Then, iteration algorithms as Monte Carlo are used to solve the Bloch-Torrey, thus simulate the MRI signal. Therefore, depending on the diffusion significance, two regimes has been establish: Static dephasing Regime and Narrowing Diffusion Regime. But, first of all an introduction to diffusion is presented.

- Diffusion is based on how the particles move through local field inhomogeneities created by perturber objects. In general, by having a number of nucleus at the same initial position, they will finally spread out over time. If a random walk movement is assumed for each spin (Fig 11), after a time T, the position of each spin will create a Gaussian distribution with a certain standard deviation (statistical physics). This standard deviation is known as the diffusion length $L_D = \sqrt{2dDT}$ where d is the dimension of the diffusion movement and D is the diffusion coefficient that depends on the medium. In other words, the nucleus will move a distance on the order of L_D equally likely in every dimension during a time interval T.

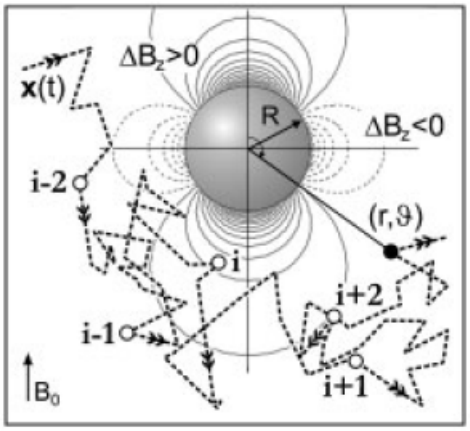

Figure 11: Spin random walk through local field inhomogeneities created by the spherical object. Along the trajectory, the spin is *feeling* different values of ΔB_z.Figure from [13].

On the other hand, the magnetic dipole moment create by the perturber will generate local field inhomogeneities $\Delta B_z(r,\theta)$ (where r and θ are spherical coordinates between the spin's and the object's location) in the main magnetic field. Thus, local differences in the nuclear frequency will appear. These local differences in the frequencies are dependent on the geometry of the perturber. One of the easiest geometries to study analytically is the sphere. The external frequency shift created by the sphere is given in Equation 11,

$$\omega_s(r,\theta) = \underbrace{\frac{4\pi}{3}\cdot\gamma\cdot\Delta\chi\cdot B_0}_{\delta\omega_s}\cdot\underbrace{\left(\frac{R}{r}\right)^3\cdot(3\ cos^2(\theta)-1)}_{Dipole\ effect\ of\ the\ sphere} \tag{11}$$

where $\Delta\chi$ is the change susceptibility between the sphere and the medium, R is the radius of the sphere and $\delta\omega_s$ is the called characteristic frequency shift.

Now a relation between the two regimes is presented. In 1994, the static dephasing regime condition was obtained by Yablonskiy and Haacke [10] as:

$$(\varrho\cdot\delta\omega)^{-1} << \frac{(\overline{r}/2)^2}{2dD} \tag{12}$$

where ϱ is the relative volume fraction (net volume of the perturbers divided by the net volume of the perturber and the tissue), $\delta\omega$ is the characteristic frequency shift,$\overline{r}$ is the average distance between the nearest particles, d is the dimension of the diffusion movement and D the diffusion coefficient of the medium. But, if the average distance between objects is of the order of the object's average radius ($\overline{R_0}$), the equation becomes [10]:

$$\frac{\overline{R_0}^2}{6}\cdot\frac{\delta\omega_s}{D} >> \varrho^{-1/3} \tag{13}$$

Notice that the exponent of the volume fraction comes from the $1/\overline{r}^3$ dependence of the spherical particles [10].

To conclude, if during a pulse sequence all the spins have experience all the magnetic field distribution due to diffusion (as in Fig 11) , the total phase of the system loose coherence. Then, there is an extra contribution to signal decay due to diffusion. In this case, the motional narrowing regime is ruling (MNR or NDR, narrowing diffusion regime). On the other hand, if each spin has felt a completely different magnetic field distribution, then each spin experiences a constant magnetic field, thus a constant phase. This is the case for when the diffusion length is much smaller than the particle diameter (diffusion is neglected) and there the signal decay can be assumed mono-exponential (dephasing due to field inhomogeneities). In this case, the static dephasing regime is ruling (SDR).

E. Transverse relaxation rate dependencies

In previous sections, the importance of ΔR_2^* and ΔR_2 to study the vessel size has been explained. Now, how these two functions depend on certain parameters is reviewed. These parameters will be factors as the echo time (TE), the main magnetic field (B_0) and differences

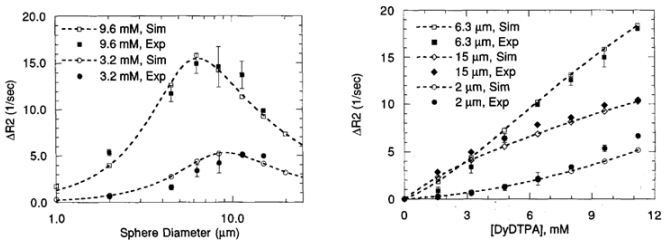

Figure 12: Transverse relaxation relaxation rate in SE sequence dependence with $\Delta\chi$. On the right image, Monte Carlo simulations and experiment were done for different concentration of contrast agent. The left image shows the relation between ΔR_2 and the sphere diameter with two different concentration of contrast agent, thus different $\Delta\chi$. Both images are extracted from [7].

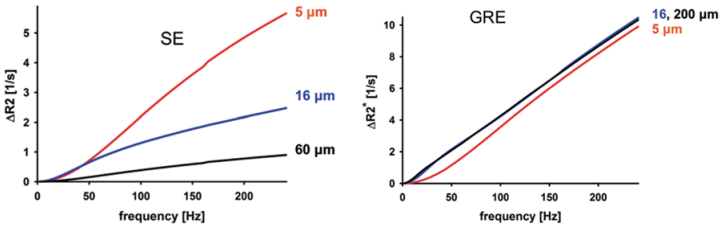

Figure 13: Relaxation rate changes as a function of the diameter of the vessels for different frequency shift ($\delta\omega$) and sequence. In the x-axis it appear the frequency shift values that are directly define by the change in susceptibility or the main magnetic field ($\delta\omega \propto \Delta\chi \cdot B_0$).

in magnetic susceptibilities ($\Delta\chi$) among others. Most of these dependencies in SE sequences for sphere perturbers where studied by Weisskoff et al in [7]. The more relevant parameters for this project are explained in this Section.

- Main magnetic field, B_0:
  The dipole-dipole interaction model explained by Bloembergen Purcell and Pound [14] predicted that R_2, thus R_2^*, should be independent of the main magnetic field. For low B_0 this prediction applies, but at high magnetic fields where diffusion and susceptibility effects are emphasize, the model does not apply. Experiments summarized by Uludag et al in [15] showed that both relaxation rates, R_2 and R_2^*, increase as the main magnetic field increases.

- Magnetic susceptibility:
  The changes in magnetic susceptibilities on a sample come from the difference between the magnetic properties of its components. By adding a contrast agent in a sample, the susceptibility change increases linearly with the concentration in mM of the added contrast agent ($\Delta\chi \propto [C]$). This relation was shown experimentally and computationally by Weisskoff and Boxerman in [7]. Figure (12) shows their results.

  Moreover, in Figure (12) left, the ΔR_2 peak is both increased and shift to lower diameters as the contrast agent concentration is increased. The fact that the relaxivity peak is achieved at lower diameters is due to the diffusion effect. In other words, the ΔR_2 reduction due to motional averaging (or narrowing diffusion) happens for lower diameters if the change in magnetic susceptibility increases. So, increasing the magnetic susceptibility $\Delta\chi$ shifts the SE curve up and to the left.

- Pulse sequence:
  In section II C, both principal pulse sequences are explained. The dependence of the relaxation rates comes from the nature of these sequences. The main difference between the two sequences is the spin rephasing method. In SE, the rephasing is done with a 180-degree pulse which reverse all the dephasing effects created by the presence of field inhomogeneities or susceptibilities effects. Then, R_2 information can be extracted. Otherwise, in GRE, the rephasing method is done with a gradient. This gradient only reverses the effects created by the dephasing gradient applied prior to it. In this case, R_2^* information can be derived. In 2009, Uludag et al. [15] studied the dependence of the relaxation rates for each sequence for different vessel sizes. A few years later, the same Uludag upgrade his work in a book [16] where the following pictures can be found (Fig 13). In this case, cylinders perturbers where considered instead of spheres.

  In the case of small vessels, both sequences give the same relation. The reason of that behaviour is diffusion. In this regime, the diffusion is fast enough to prevent the 180-degree pulse from recover the R_2^* effects. For big vessels, both sequences have different behaviours. For SE, at a fixed frequency shift, bigger vessels have lower ΔR_2 values (Fig 13 left). This occurs because the 180-degree pulse recovers all the signal lost on dephasing, canceling out phase dispersion. Then, a higher sensitivity in terms of relaxivity rates is obtained for small and medium vessels. For GRE, ΔR_2^* becomes independently of the vessel size (Fig 13 right). In this case, diffusion becomes unimportant and the signal loss is ruled by intravoxel dephasing.

- Echo time:
  Boxerman and Weisskoff studied the effect of the TE on the relaxation rate for SE sequences in cylinders [8]. They found that for low TE both, the ΔR_2 peak and the vessel size at which the peak occurs, decrease. This effect can be seen in Fig (14).

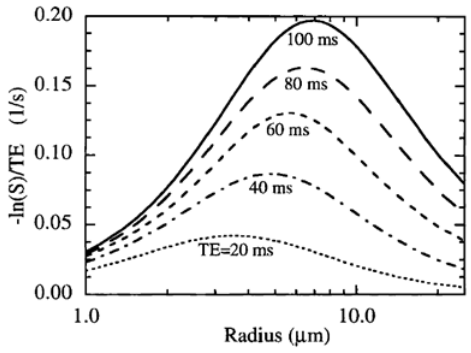

Figure 14: Relaxation rate dependence ΔR_2 on the echo time (TE) for cylinders in a SE sequence. Image from 8

III. METHODOLOGY

A. Thesis objectives

The objective of this thesis is to study a relation between the vessel size and the changes in the relaxation rates in a 7T Philips MRI machine. As mention in the introdution, Boxerman et al.[7] have shown a peak in relaxation time at a 5um radius size for 1.5T. Proofing this relation but at 7T is the main objective of the thesis. However, the scope of the project has been reduced to three main challenges due to time-line restrictions and difficulties along the development of the work.

- The first challenge was to build different imaging phantoms (specifically designed objects) to be scanned in a 7T MRI machine, to evaluate, analyze, and tune the performance of the machine itself.

- The second challenge was to design a MATLAB code which was capable of calculating the transverse relaxation rate for each pixel of the image obtained from the 7T scanner after performing a Multi gradient-echo sequence. This was necessary to characterize the phantom.

- The third challenge was to perform the multi gradient-echo sequence of 5 echoes at the 7T scanner and then processing the data using the MATLAB code mentioned above. After that, a transverse relaxation rate for each component of the phantom was obtained.

B. Phantom Design

Different phantoms designs were made during this project. An overview of all its components is given in this section.

1. Buffer solution composition

The chemicals used are Dysprosium(III)chloride hexahydrate (Adrich's supplier), Diethylenetriaminepentacetic acid (DTPA, Alfa Aesar supplier), Sodium acetate trihydrate (Sigma supplier) and distillate water. The Sodium acetate trihydrate was introduced to reduce the pH of the solution to 5.5 and avoid the Dysprosium to precipitate. The molar concentration of the Dy-DTPA in the solution was set at 5mM and, like this, reducing the magnetic susceptibility of the solution. The magnetic susceptibility of a mixture ($\chi_s ol$) is given by the Wiedemann's additivity law:

$$\chi_{sol} = 4\pi \sum_i c_i \chi_{\mathrm{M}}(\mathrm{i}) \tag{14}$$

where i represents the components of the solution, c_i is the molar contentration in mM and $\chi_{\mathrm{M}}(\mathrm{i})$ is the molar susceptibility of the *ith* component in (cm^3/mol).

For this experiment, [Dy-DTPA]=5mM and $\chi_{\mathrm{M}}(\mathrm{Dy-DTPA}) = 0.047\mathrm{cm}^3/\mathrm{mol}$ [13], so the magnetic susceptibility of the mixture was:

$$\begin{aligned}\chi_{\mathrm{sol}} &= \chi_{H_2O} + \chi_{Dy-DTPA} = \\ &= -9.060 + 4\pi[Dy-DTPA]\chi_M(Dy-DTPA) = \\ &= -9.060 + 4\pi \cdot 5 \cdot 0.047 = \\ &= -9.060 + 2.953 = -6.107\mathrm{ppm}\end{aligned} \tag{15}$$

So, the magnetic susceptibility of the solution was set at -6.1ppm.

2. Spheres

Two types of spheres were used during the experiments.

- Duke standard glass microspheres. Two different diameters were used, 1.9μm (catalog number 9002) and 32.5μm (catalog number 9030). For more information [17].

- CC standard Polystyrene Latex microspheres. Four diameters were used in this case, 3μm (particle number 6602793), 10μm (particle number 6602796), 20μm (particle number 6602798) and 30μm (particle number 6602799). For more information [18].

3. Phantom structure

The structure of the phantom was build into two parts. The container was a tube of 12.5cm of diameter made of PVC (PolyVinyl Chloride).

Figure 15: Phantom container.

For the inside, two different platforms were created:

1. Circular platform (Fig 16): This design had the same direction as the PVC tube, allowing us to insert the tubes with the microspheres parallel to the main magnetic field. The screws that put together the legs and the circular part were of Nylon material.

Figure 16: Circular platform.

2. Rectangular platform (Fig 17): This design allowed us to insert the tubes with the microspheres perpendicular to the main magnetic field of the scanner. This platform was created using a 3D printer. The material of this platform is PLA material [19].

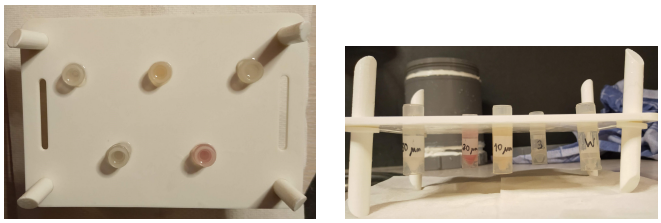

Figure 17: 3D printed rectangular design

Moreover, the external field shift (field offset) created by the tubes depends on the orientation with B_0. By defining the coordinate system as in Fig18, the magnetic field inside and outside the tube is given by [4]:

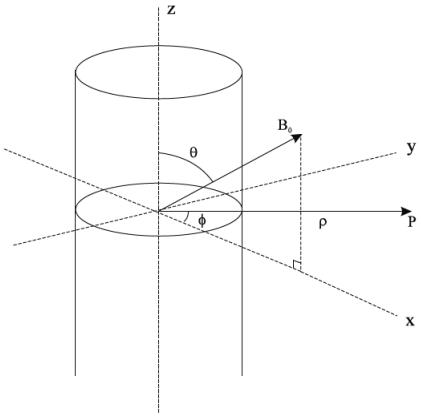

Figure 18: Representation of the cylinder with B_0 [4].

$$\Delta B_{in} = \frac{\Delta\chi}{6}(3cos^2\theta - 1)\mathrm{B}_0 + \frac{1}{3}\chi_e \mathrm{B}_0 \tag{16}$$

$$\Delta B_{out} = \frac{\Delta\chi}{2}\frac{a^2}{\rho^2}sin^2\theta cos2\phi \mathrm{B}_0 + \frac{1}{3}\chi_e \mathrm{B}_0 \tag{17}$$

where χ_e represents the susceptibility outside the tube, $\Delta\chi = \chi_i - \chi_e$ is the magnetic susceptibility difference between inside and outside the tube, a is the radius of the tube and ρ is the distance at which we evaluate the field shift.

In the parallel case, $\theta = 0$, both internal and external magnetic shift have the same value $\Delta B_{in} = \Delta B_{out} = \frac{1}{3}\chi_e \mathrm{B}_0$. So, all the values have the same offset. For the perpendicular case, $\theta = \pi/2$, $\Delta B_{in} \neq \Delta B_{out}$. Then, the minimum distance required to not be affected by the field offset of the next tube (reduction of the 90%) is:

$$\begin{aligned}\Delta B_{ext} &= \mathrm{B}_0\left(\frac{\Delta\chi}{2}\frac{a^2}{\rho^2} + \frac{\chi_e}{3}\right) = \\ &= \mathrm{B}_0\frac{\Delta\chi}{2}\frac{a^2}{\rho^2} + K\end{aligned} \tag{18}$$

So,

$$\frac{a^2}{\rho^2} = 0.1 \rightarrow \rho = \frac{0.5\mathrm{cm}}{\sqrt{0.1}} = 1.6\mathrm{cm} \tag{19}$$

This distance is needed in the case where the tubes are perpendicular to the main magnetic field. For that reason, the rectangular platform was design with a 5cm radial separation from each hole.

C. Phantom Characterization: Multi-Gradient Echo and MATLAB data processing

In order to characterize the phantom, a Multi gradient echo sequence was applied (see AppendixB for specifics). The aim of this sequence is to obtain a R_2^* value for each component of the phantom. From section II B we know that the signal obtained from the scanner is proportional to $e^{-R_2^* \cdot t}$. So, if a Multi-GRE sequence of 5 echoes is applied, one signal value per echo is obtained. Then, a regression of these five values can be done to obtain the R_2^* value for each voxel of the phantom. To get that, the data from the scanner is imported to MATLAB. A mask is applied by using the Segmentation Tool. In this project, two masks were used. One including just the inside of the tubes without touching the edges, and the other one including the entire tube and a part of the vicinity. Then, a fitting is performed. But, instead of doing an exponential fitting to obtain the transverse relaxation rate, a logarithmic transformation to perform a linear fitting is used (see Equation 20).

$$S \propto e^{-R_2^* \cdot TE} \rightarrow ln(s) \propto -R_2^* \cdot TE \tag{20}$$

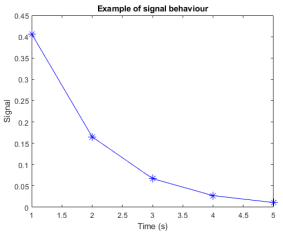

(a) Example of ideal signal dependence versus echo times. The five echo times are represented with the asterisk symbols.

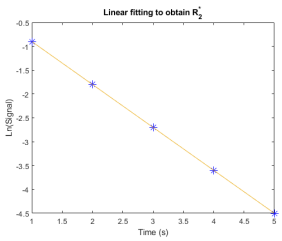

(b) Example of linear regression after applying the logarithm to the signal values. The regression is a first order polynomial $y = ax + b$, where $R_2^* = |a|$.

Figure 19: Matlab example of how to extract a R_2^* value for each voxel.

Then, every pixel of every slice of the phantom scan has a R_2^* value obtained by the example regression shown in Figure(19b). So, with all these values, a R_2^* histogram for each component of the phantom was performed. The value with the maximum number of counts should be the relaxation rate that correspond to the chosen tube.

IV. RESULTS AND DISCUSSION

In this section, all the phantom experiments done for this thesis will be explained and discussed. In the first experiment an inherit phantom design and glass micro-spheres were used. A new phantom designed specifically for this project was presented in the second experiment. Moreover, polystyrene micro-spheres were needed because of its lower density. Finally, a last experiment was performed were changes in the phantom platform and the volume fraction of the micro-spheres were adopted.

1. Inherit phantom design

In this experiment, a different phantom obtained from the Radio-pharmaceutical department was used (see Fig (20).

Figure 20: Phantom used in the first experiment.

In this case Duke glass micro-spheres of two different sizes, 1.9μm and 32.5μm, were used [17]. In total 8 different samples were made to do the scan. The specifics of these tubes are shown in Table (II).

Table II: Specifications for the samples of the first phantom experiment.

Samples:	32.5(μm)	1.9(μm)	buffer	water
1	53.2 mg		x	
2	258.0 mg		x	
3		51.5 mg	x	
4		256.3 mg	x	
5			x	
6			x	
7				x
8				x

This phantom was inserted in the MRI scanner with the sample tubes perpendicular to the main magnetic field. The Multi Gradient-echo scan used the following scan parameters:

- -Data dimension of [480, 480,72 ,5] ([x pixels, y pixels, slices, echoes]),
- TE=[8, 21, 33, 46, 58] msec,
- Spatial resolution $\Delta x \Delta y = 0.5$mm
- Slice thickness of 1mm.

First of all, an example of intensity image is shown in Fig(21).

It is shown from the previous image that at larger echoes, the more distortions appear in the image.
Secondly, the dipole effect was observed as it shows Fig(22). The dipoles created by the water tubes (number 7 and 8) are stronger due to the difference in susceptibility between inside (water) and outside (buffer solution) the tube. Moreover, it can be seen that the rest of tubes

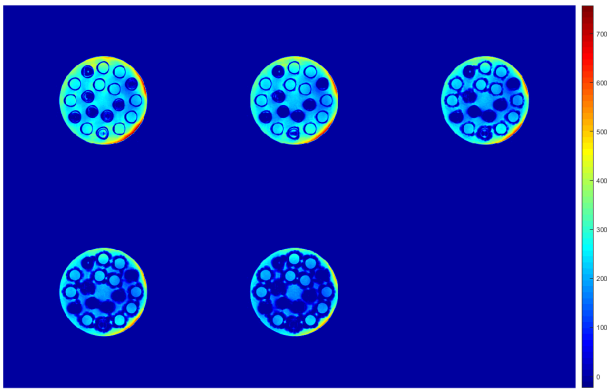

Figure 21: Five echoes obtained from the Multi Gradient-echo sequence for a middle part (Fig38) slice (slice number 42). The first echo is on the top left part of the image and the 5th echo is on the bottom right part. The color map represents the intensity of the signal. Blue colors are low intensity and red colors are high intensity.

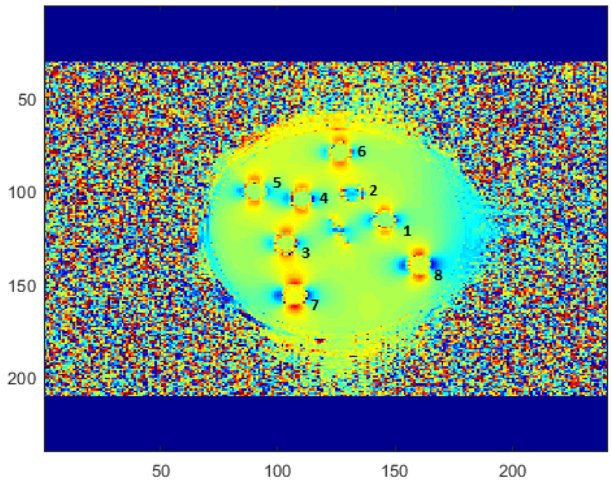

Figure 22: Dipole effect since the tubes are placed perpendicular to B_0 [4]. The numbers that appear in the image correspond to the samples in Table II. Each number make reference to the tube on the left side of them.

on Fig 22 present almost the same dipole effect even that the size and volume fraction of micro-spheres in it is different. Since a slice from the middle part of the sample tube (see Fig38) is represented, different dipole field perturbations for each tube were expected. In this region of the tube, the spheres should be distributed uniformly and randomly thus creating a perturbation field relative to the volume fraction and size of the spheres of each tube. Since all the field distortions created by the sample tubes with micro-spheres are similar, depending on the sample because the micro-spheres are indeed changing the susceptibility of the inside of the tube.

Table III: Specifications for the samples with micro-spheres of the second phantom experiment. d represents the diameter of the spheres, V_{pb} is the volume extracted from the bottle containing the micro-spheres, V_s is the volume of spheres in the tube and ϱ is the volume fraction. The total volume of the sample tubes is $V_t = 1.78$mL

d(μm)	V_{pb}(mL)	V_s(mL)	ϱ(%)
3	3	0.00025	0.015
10	1.5	0.0015	0.08
20	1.5	0.0076	0.43
30	1.5	0.025	1.43

Finally, a mask for each tube was created to obtain the R_2^* value for each sample. After checking the procedure the following problems were found:

1. The micro-spheres were too heavy ($\rho = 2.5$g/cm^3). The density of the buffer solution can be considered 1g/cm^3 since most of it is water. So, the spheres were settling down fast enough to see the signal. So the scanner was detecting a signal coming from an aggregation of spheres (the same as having just one huge sphere), not from all the spheres individually.
2. The cavity that was holding the tubes created distortions in the images. Moreover, the tubes were not still at the same height due to the phantom structure.
3. There was air bubbles in the tubes that created huge distortions in the images.

2. Circular platform design

After the problems had in the previous experiment, the phantom itself and the spheres were changed. In this case, the spheres were made of polystyrene [18] and the phantom used is shown in Fig(15-16). Polystyrene has a lower density than glass, $\rho = 1.05$g/cm^3. For this experiment 6 sample tubes were used. Four of them had micro-spheres, one with pure water and one more with buffer solution. The properties of the samples with micro-spheres is summarized in Table(III).

The phantom was introduced with the sample tubes parallel to the main magnetic field. The scan parameters used in this multi gradient-echo experiment are:

- Data dimensions=[480,480,78,5]
- TE=[8,20.5,33.1,45.6,58.2]msec.
- Spatial resolution, $\Delta x = \Delta y = 0.5$mm.

- Slice thickness=1mm.

The signal map for a certain slice from the middle (i.e 48) part (slices 46-50) of the sample tube is shown in Fig(23). The qualitative distribution of the tubes is shown in Fig(39).

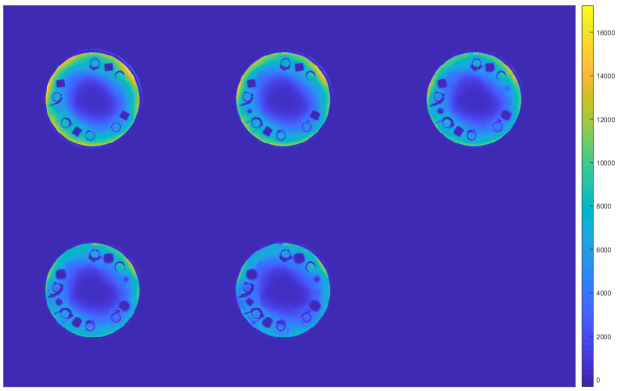

Figure 23: Multi Gradient-echo data for slice 48 of the phantom. First echo corresponds to the top left image, and last echo to the bottom right image.

Moreover, before processing the data and calculate the relaxation rate maps, the B_0 field was checked on homogeneity. Fig 24 is an example of homogeneity in B_0 obtained by the scanner after shimming. Shimming is the process by which the main magnetic field (B_0) is made more homogeneous. In our scanner, active shimming is performed. It consists on using currents directed through certain coils to generate a "corrective" magnetic field. The theory underlying the shimming method is based on spherical harmonic analysis. Any field can be expanded into a sum of a constant field of magnitude B_0 and weighted terms reflecting each spherical harmonic component (Equation 21).

$$\begin{aligned} B_{\text{actual}} = & B_0 + (3 \text{ linear harmonics}) + \\ & + (5 \text{ second order harmonics}) + \\ & + (7 \text{ third order harmonics}) + \cdots \end{aligned} \tag{21}$$

Then, for each unwanted spherical harmonic component in the uncorrected magnetic field (B_{actual}), a carefully controlled supplemental magnetic field is generated by passing current through an active shim gradient. This supplemental shim field has the same spatial distribution, but is equal and opposite to the unwanted component. By super-positioning and merging these two opposite magnetic fields together, a neutralization and cancellation of the magnetic field error (inhomogeneity) is effected.
Since the tubes are placed parallel to the main magnetic field, no dipole effect appears in the image (Chapter 25,[4]).

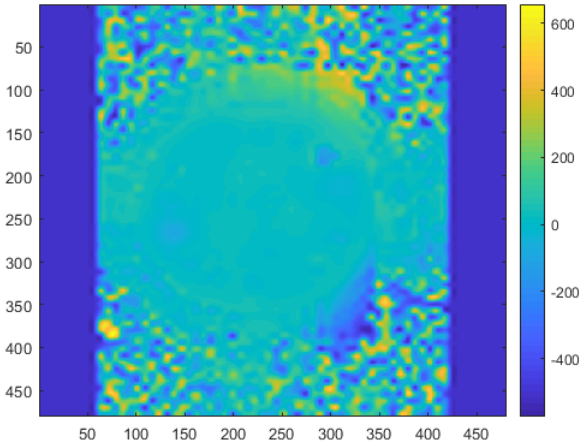

Figure 24: B_0 shimmed field map for Experiment 2. Slice 48.

Table IV: Maximum $R_2^*(1/s)$ values for all the sample tubes obtained from the histograms in Fig25 and 26

3μm	10μm	20μm	30μm	buffer	water
9	8	17	15	6	2

Then, a $R_2^*(1/s)$ map for each sample tube was performed. The results are shown in Figure 25-26.

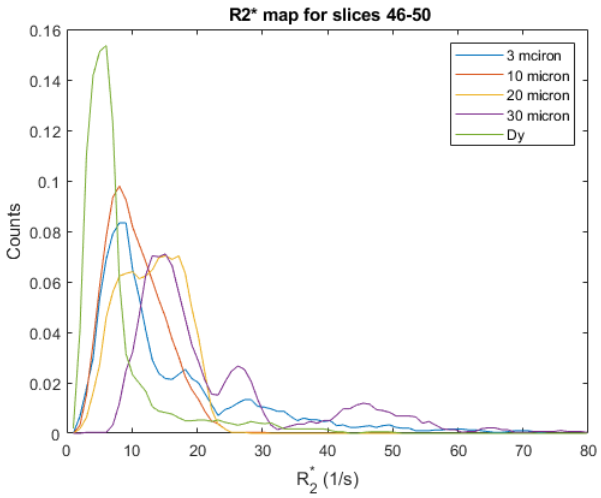

Figure 25: $R_2^*(1/s)$ maps for each micro-spheres sample tube and the buffer tube (slices 46-50). Color specification: Blue to 3μm, Orange to 10μm, Yellow to 20μm, Purple to 30μm and Green to buffer.

First of all, the R_2^* values for water and buffer tubes seemed consistent. Adding a paramagnetic agent contrast (Dy-DTPA in this case) to water decreases its magnetic susceptibility. It goes from -9ppm to -6ppm (see Section III B), thus the relaxation rate R_2^* increases.

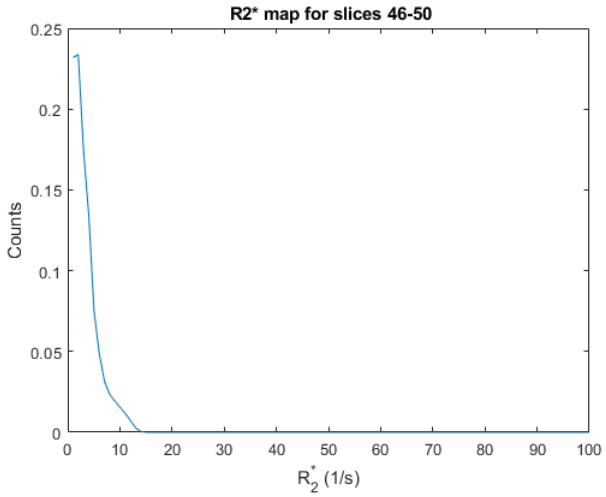

Figure 26: $R_2^*(1/s)$ maps for water tube (slices 46-50).

In this experiment, the relaxation time found for water is lower than for the buffer solution.

Secondly, it can be seen from Table IV that the relaxation rates for the tubes with micro-spheres do not behave as predicted (see GRE shape in Fig 1). The ΔR_2^* for this experiment is obtained by subtracting spheres and buffer transverse relaxation rate. The results are plotted in Fig 27.

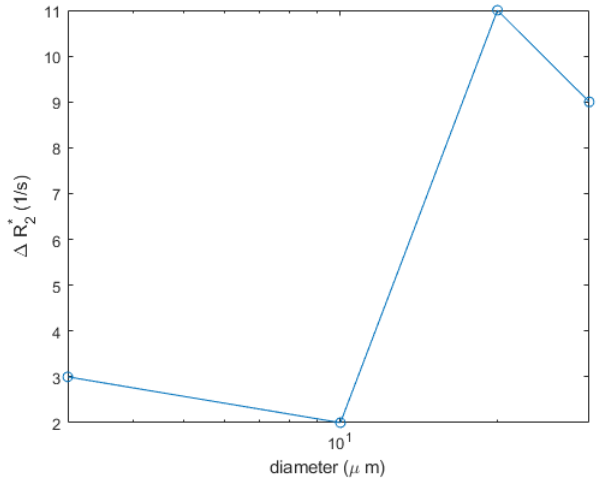

Figure 27: $\Delta R_2^*(1/s)$ and particle size relation for Prototype 2.

Because of the behaviour detected in Fig 27, the data was inspected pixel by pixel for these tubes and a non-decaying behaviour of the signal was observed. In Section III C, it is assumed a mono exponential decaying behaviour for the signal to calculate R_2^*. So, if this assumption is not fulfilled, the fitting of the signal loses rigor. One possible reason for this evidence can be the chosen echo times. Experimentally, the signal does not decay mono exponentially, but in most of the cases this assumption is valid. On the other hand, if the echo times are too short, then the signal that is measured can be affected by the called "shoulder" effect. In this region, the signal does not behave as declared, thus the fitting done is useless.

Finally, a summary of the issues acknowledged in this experiment is presented:

1. The volume fraction of the tubes was not the one proposed. An ideal constant volume fraction of $2-3\%$ was necessary, however, experimental results show otherwise (see Table III). The calculation for these values is shown in Appendix D.

2. The tubes were inserted parallel to the main magnetic field so that the micro-spheres where settling down on the short length of the tube. So, a faster aggregation of them is appearing.

3. The poor fitting obtained for some pixels can be fixed by increasing the echo times. This experiment was performed using the following echo times: $TE = [10, 40, 70, 100, 130]msec$. The R_2^* histograms for the tubes at this larger echo times were similar, thus no advantage in terms of signal fitting was obtained. Additionally, it was shown more clearly that some regions of the prototype were creating large distortions in the image that were affecting the tubes. The distortions were created from the Nylon screws of the platform that have a high magnetic susceptibility.

3. Rectangular platform design

In this last experiment, a rectangular platform has been designed and 3D-printed (see Fig(17)). The samples were inserted perpendicular to the main magnetic field. In this case, 5 tubes were present. Four of them were filled with micro-spheres (see TableV) and the remaining one was set as a control sample (water solution). The distribution of the tubes can be seen in Fig(40). The distance between the tubes is 5 cm to avoid external field shifts affecting one tube to another (see Section III B).

The Multi Gradient-echo parameters for this scan were:

- Data dimensions=$[480, 480, 52, 5]$.
- TE=$[10, 22.5, 35, 47.5, 60]$msec.
- Spatial resolution, $\Delta x = \Delta y = 0.5$mm.
- Slice thickness=1mm.

For this last experiment, a detailed analysis of all the variables was performed in order to check all the possible causes for the mismatch between the results

Table V: Specifications for the samples of the third phantom experiment. d represents the diameter of the spheres, V_{pb} is the volume extracted from the bottle containing the micro-spheres, V_s is the volume of spheres in the tube and ϱ is the volume fraction. The total volume of the sample tubes is $V_t = 1.78mL$.

d(μm)	V_{pb}(mL)	V_s(mL)	ϱ(%)
3	10	0.00082	0.05
10	10	0.010	0.56
20	10	0.051	2.86
30	3	0.051	2.86

and theoretical analysis.

First of all, the B_0 shimmed field map was checked to see if meaningful inhomogeneities were present. In other words, the shimming was performed correctly by the scanner. The B_0 field obtained directly from the scan has a data dimensions of a lower resolution in comparison with the data resolution obtained from the Multi Gradient-echo sequence. Then, resize and an interpolate was needed to compare both images. The initial characteristics of the B_0 field map data were:

- Data dimensions=[64,64,35].
- Spatial resolution, $\Delta x = \Delta y = 3.75$mm.
- Slice thickness=3.75mm.

Then, after resize and interpolating, Fig(28) was obtained. The sample tubes created dipole field patterns that depend on the difference in susceptibility and the shape and orientation of the object. In this case, the dipole perturbation appeared in the image because of the orientation of the tubes (perpendicular to B_0, [4]). Moreover, when an histogram through all the slices is performed (Fig29), a B_0 of -8.96 ± 30.01Hz was obtained. This distribution can be assumed as homogeneous.

Moreover, an example of signal map for this experiment is shown in Fig 30.

Secondly, the R_2^* value for the buffer solution ($H_20 + Dy - DTPA$ 5mM) was calculated. To do so, a region of interest (ROI) of the phantom, where no sample tube was located, was chosen. After applying the MATLAB procedure explained in Section III C, an histogram over all the slices (since all of them contain buffer solution) of the phantom was performed (Fig 31). The peak on the histogram correspond to a $R_2^* \approx 5.5(1/s)$. This value do not differ from the value obtained in Experiment 2, thus may be correct.

Thirdly, the histogram from the control sample (water) tube was performed (Fig 32). In this case, two peaks appeared. The first peak is around $R_2^* = 5.5(1/s)$ and the second one around $R_2^* = 50(1/s)$. Since slices concerning both buffer solution and water were taken into account to perform the histogram, it can be conclude that the first peak correspond to the buffer solution since it matches

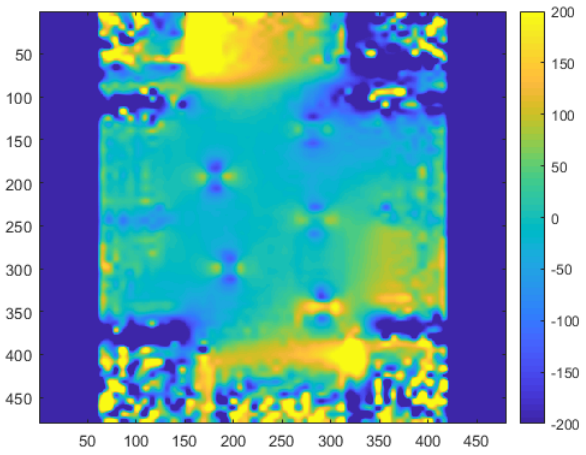

Figure 28: B_0 field map. Phantom slice number 20. Color range values goes from -200Hz to +200Hz. The sample tubes created a dipole pattern with the negative lobes in the vertical axis and the positive lobes in the horizontal axis. This shows that the B_0 field is going towards the horizontal axis.

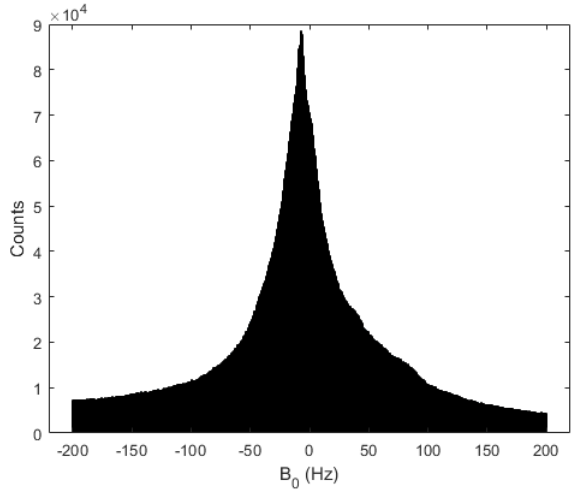

Figure 29: B_0 field map histogram of all the slices after shimming.

the other results. Otherwise, the second peak, referred to water, has a large discrepancy with the results from circular platform phantom. A possible explanation is the presence of air bubbles enclosed in the tube. This bubbles were acknowledged after the experiment.

After checking all fundamental parameters, the transverse relaxation rate was measured for the tubes. The same procedure as in Experiment 2 was followed to obtain Fig 33. In this case, all the tubes present the maximum value at $R_2^* = 5.5(1/s)$.

Since the results were the same than the previous experiment, the region of interest is now expanded to the

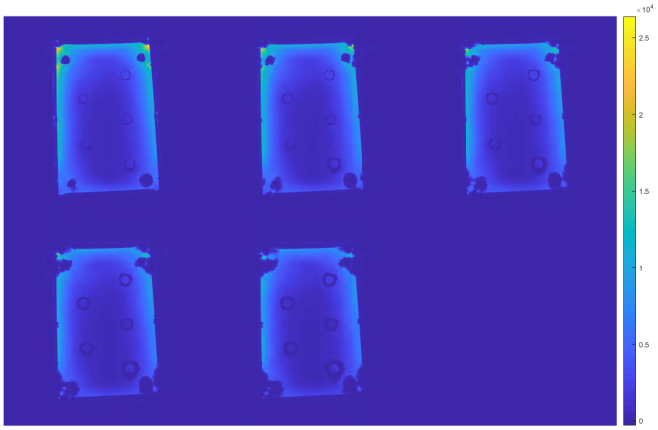

Figure 30: Multi Gradient-echo data for slice 20 of the phantom. First echo corresponds to the top left image and last echo to the bottom right image. Water distortion through the echoes is seen.

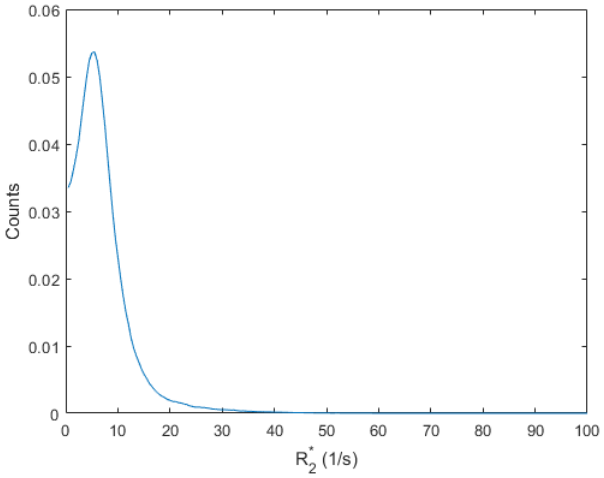

Figure 31: Transverse relaxation rate histogram for the solution ($H_20 + Dy - DTPA$).

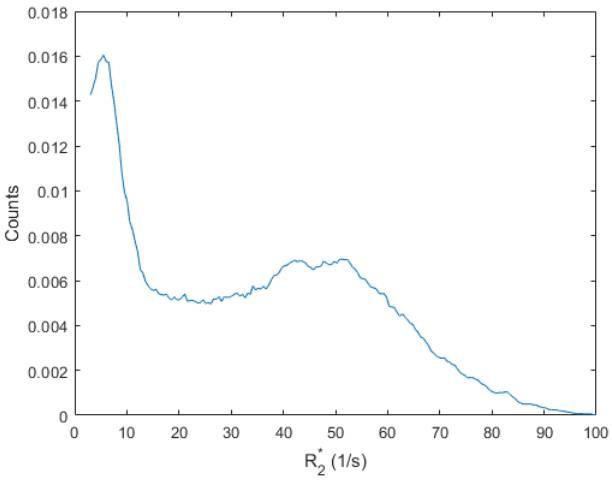

Figure 32: Transverse relaxation rate histogram for the water tube. Slices 10 to 30 were used.

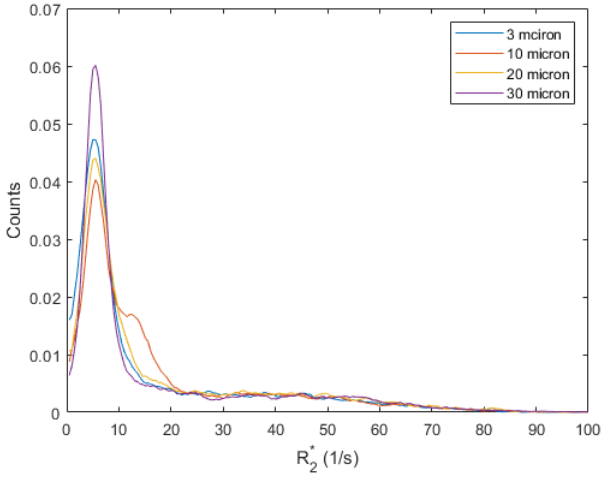

Figure 33: Transverse relaxation rate histogram for tubes filled with micro-spheres. Slices 18 to 22 were applied. Color specification: Blue to 3μm, Orange to 10μm, Yellow to 20μm and Purple to 30μm.

height of the tube. Three regions of the tube were analyzed so that the effect of the micro-spheres was reviewed in more detail. The tubes were divided as it shows Fig(38) (see Appendix). The slices corresponding to each part were chosen by looking at the volume image of the tubes:

a Top part: Slices 23-27.

b Middle part: Slices 18-22.

c Bottom part: Slices 13-17.

The interest was in the middle part where a random distribution of the micro-spheres was expected. The top part has the cap which can keep air bubbles if the closing is not carefully done. The bottom part has this cone shape where the micro-spheres can aggregate easily.

So, a total of 15 slices (around 1.5cm of the sample tubes) were selected. Then, a R_2^* histogram for each tube and slice was obtained Fig(34).

A series of facts can be discussed:

1. The histograms of the slice 27 for 3 and 20 μm spheres and the histograms of the slices 16 and 17 for 30 μm do not appear in Fig(34). The reason for that was the R_2^* range demanded to plot the five histograms in one graph. The range declared for every group of five was defined in terms of the first slice of the group. So, for the bottom group

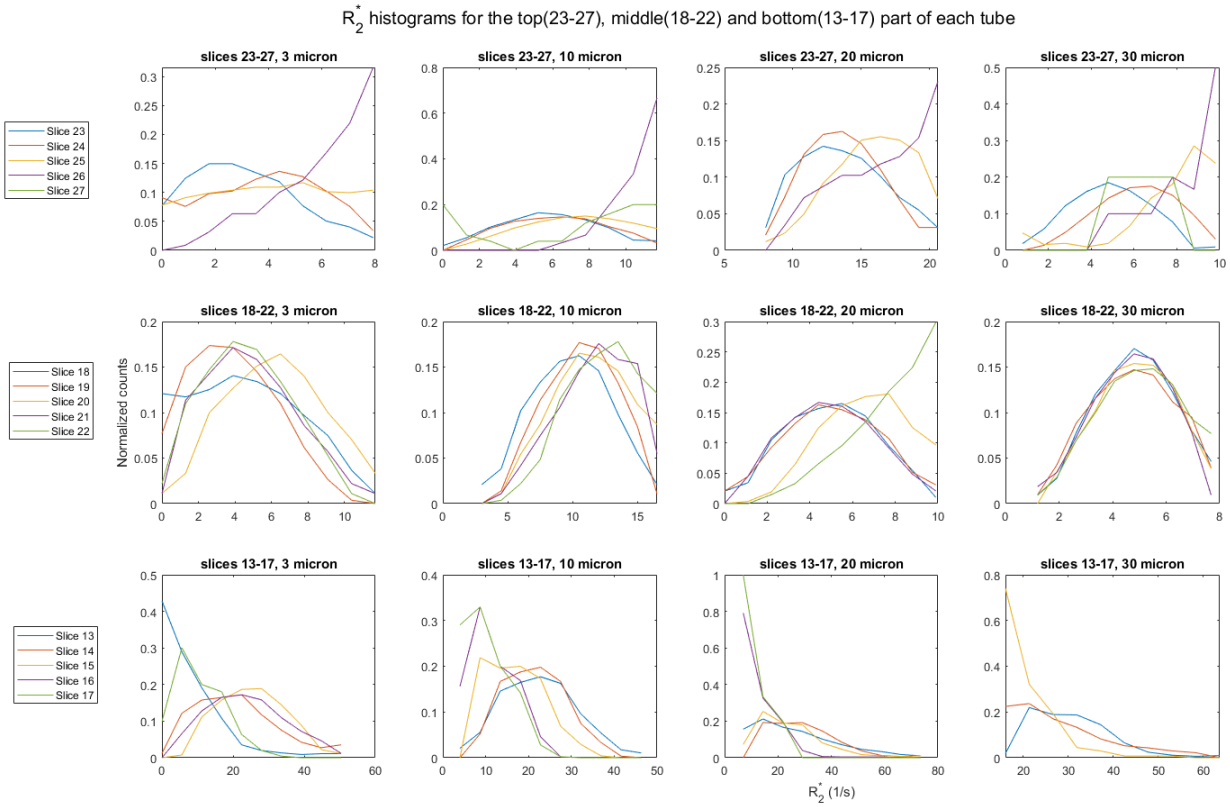

Figure 34: $R_2^*(1/s)$ values for all the slices selected in each sample tube.

of slices (13-17), the x-range to plot the five histograms was chosen using slice number 13. Then, if a slice does not operates in this entire range, no histogram is plotted. This method was used for the histograms to be compared. The only way to compare histograms is for them to have the same bin-vector.

2. All the histograms were awaited to have a Gaussian distribution with its peaks representing the most repeated value found in the R_2^* map.

3. The histograms for the middle part of the 10μm size seems to disagree with Fig 33. The peak is displaced from the center value, $5(1/s) \rightarrow 10(1/s)$. Checking closer, the 10μm histogram has another small peak between $10-20(1/s)$ that can be showed in the slice by slice histogram clearly.

4. The R_2^* histograms of the bottom part are larger in comparison of the other parts. A possible explanation to this evidence is that the spheres are still settling down to the bottom part of the tube.

5. The R_2^* histograms of the top part are more erratic. Slices 26 and 27 go off the expected behaviour. A possible cause is the presence of small air bubbles in the screw as it was seen for the water tube.

After all these facts in relation to the theory, it was necessary to check if the the MATLAB code was working as thought. Then, the next step was to check the R_2^* values obtained from the MATLAB fitting program with the R_2^* values obtained directly from the Philips scanner. The same mask selecting the sample tubes was applied to both data. In this case, the ROI for each tube included the whole tube and a part of solution, to make sure that everything happening inside the tube was considered. Moreover, all the slices were included in the histogram. The results are shown in Fig(35) and Fig(36). Both histograms look the same, thus the MATLAB program is operating correctly. Then, a coding problem can be ruled out.

V. CONCLUSIONS

The goal of this project was to calculate, experimentally at 7T, the behaviour of the transverse relaxation rates ΔR_2 (Spin echo sequence) and ΔR_2^* (Gradient echo sequence) in presence of microspheres. More specifically, to measure the dependence between the ΔR_2 and ΔR_2^* in terms of the diameter of the spheres. This relation was introduced in an analytical way by Yablonskiy and Haacke [10] in 1994. A year later, experimental results at

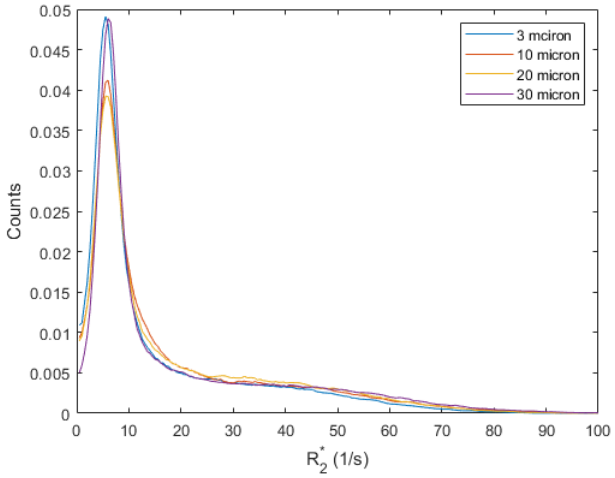

Figure 35: $R_2^*(1/s)$ values for all sample tubes with micro-spheres obtained from the MATLAB program. Legend: blue:3μm, orange:10μm, yellow: 20μm and purple:30μm.

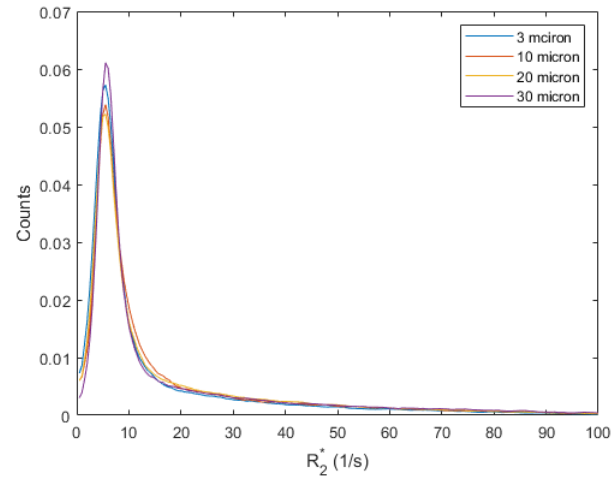

Figure 36: $R_2^*(1/s)$ values for all sample tubes with micro-spheres obtained from Philips scanner. Legend: blue:3μm, orange:10μm, yellow: 20μm and purple:30μm.

a main magnetic field of $1.5T$ were presented by Weisskoff [7] and Boxerman [8]. In 2014, Troprs et al.[9] showed Monte Carlo simulation of the wanted relation for different main magnetic fields using cylinders to mimic the vessels. All this work was done under the Static dephasing regime condition where diffusion effects may be ignored. For capillaries (small vessels of sizes between $5-10\mu m$) diffusion phenomena can not be ignored. For this case, the Narrowing diffusion regime applies. The analysis in this region becomes difficult to solve both analytically and experimentally. For that reason, most of the literature is focus on solving the dependence under the Static dephasing regime, ignoring diffusion phenomena. For this project the same assumption was used. After the experiments explained in Section IV, the following conclusions and solutions to be applied in further work were conclude:

- **Regime**: The SDR was assumed in order to obtain and describe the results. Since the goal of this project is to perform the experiment for small vessels (microvasculature), a different theoretical approach assuming the diffusion phenomena should be useful.

- **Spheres:**

  - The settling time of the spheres needs to be reduced in order to improve the results. To achieve this some approaches can be adopt. Firstly, the density of the buffer solution should be increased. The addition of salt $NaCl$ is a possibility. In this case, the diamagnetic behaviour of this compound needs to be appraised in order to preserve the requested $\Delta\chi$ between inside and outside the tubes. Secondly, increase the solution $Dy-DTPA$ concentration of inside the tubes is also an option. Then, the larger induced field offsets around the spheres will induce a stronger R_2^* dephasing effect. Finally, using larger tubes can be helpful. For longer tubes, the spheres will take more time to settle and the area of the tube were a random and uniform distribution of the spheres can be assumed would increase.

  - A bigger range of spheres would improve the sensibility of this experiment. The sizes used in this experiment does not cover the transition between the Narrowing diffusion regime and the Static dephasing regime. More sizes of microspheres should be include to calculate the behaviour in this transition region. Thus, sizes of $4-9\ \mu m$ should be covered. Furthermore, the polystyrene spheres used in Experiment 2 and 3 tended to aggregate. This evidence was noticed while the tube mixture (buffer solution and microspheres) was performed. Under the microscope, the aggregation of the spheres was observed. So, the tubes were inserted in a ultrasonic bath to reverse the aggregation. A possible reason for this aggregation could be the old fabrication date of the sphere samples. After 15 years they could have been lost the monodispersion property.

- **Analytical approach:** To analytically estimate the transverse relaxation rate of the buffer solution, the relaxivity (r value should be calculated. Then, R_2^* can be found by using Equation(22).

$$\frac{1}{T_i} = \frac{1}{T_i^0} + r_i[C] \ ; \ i = 1, 2 \tag{22}$$

where T_i^0 is the relaxation time of the tissue in absence of the contrast agent, $[C]$ is the concentration in mM of the contrast agent and r_i is the relaxivity. Relaxivity is a measure of the sensitivity of the contrast agent and has $mM^{-1}s^{-1}$ units. Then, the r_2 for Dy-DTPA at 7T and room temperature needs to be calculate to estimate R_2^* of the solution. This information would help to the judgement of the results obtained.

After these possible improvements, the phantom experiment can be repeated. Then, once the characterization is successfully achieved, the simultaneous SE-GRE sequence can be applied to obtain the relation between the transverse relaxation rates and the diameters of the perturbers. The results obtained will be useful for different purposes. Both relations, R_2^* vs d for GRE and R_2 vs d for SE, can be used to study in further detail the growth of new vessels or the tracking of radionuclides delivery spheres for example. Moreover, the characterization of tumors or the revascularization of vessels after some therapies have been applied, are also fields of study that can be benefited by this project.

VI. LAYMAN SUMMARY

The microvasculature is the set of blood vessels with a diameter of less than 100 m. To get an idea, they are similar in size to a person's hair. If you look at the brain, these blood vessels are responsible for distributing the blood to all parts. Unfortunately, if a person suffers from brain cancer he is diagnosed with radiotherapy and / or chemo. Once the treatment has been applied, the ability of these vessels to deliver the blood can be affected. Then, being able to study the behavior of these vessels using MRI can be very helpful. In this case, a wider understanding and improvement of therapies could be achieved. In this dissertation we will focus on studying the signal that spheres produce when they are inserted into a liquid. These spheres, of different diameters, represent the blood vessels. Finally, from the signal produced by the different sizes of the spheres, it can be extracted some signal properties that will lead us to detect and see how these vessels behave in patients.

REFERENCES

[1] K. M. Schmainda, S. D. R, A. M. Joseph, R. Lund, B. D. Ward, A. P. Pathak, J. L. Ulmer, M. A. Baddrudoja, and H. G. J. Krouwer, "Characterization of a first-pass gradient-echo spin-echo method to predict brain tumor grade and angiogenesis," (2004).

[2] M. H. Zwartbol, A. G. van der Kolk, R. Ghaznawi, Y. van der Graaf, J. Hendrikse, and M. I. G. and, "Intracranial vessel wall lesions on 7t MRI (magnetic resonance imaging)," Stroke **50**, 88–94 (2019).

[3] R. Ali, M. Goubran, O. Choudhri, and M. M. Zeineh, "Seven-tesla MRI and neuroimaging biomarkers for alzheimer's disease," Neurosurgical Focus **39**, E4 (2015).

[4] R. W. Brown, Y.-C. N. Cheng, E. M. Haacke, M. R. Thompson, and R. Venkatesan, eds., *Magnetic Resonance Imaging* (John Wiley and Sons Ltd, 2014).

[5] F. Bloch, "Nuclear induction," Physical Review **70**, 460–474 (1946).

[6] I. Troprs, S. Grimault, A. Vaeth, E. Grillon, C. Julien, J.-F. Payen, L. Lamalle, and M. Dcorps, "Vessel size imaging," Magnetic Resonance in Medicine **45**, 397–408 (2001).

[7] R. Weisskoff, C. S. Zuo, J. L. Boxerman, and B. R. Rosen, "Microscopic susceptibility variation and transverse relaxation: Theory and experiment," Magnetic Resonance in Medicine **31**, 601–610 (1994).

[8] J. L. Boxerman, L. M. Hamberg, B. R. Rosen, and R. M. Weisskoff, "Mr contrast due to intravascular magnetic susceptibility perturbations," Magnetic Resonance in Medicine **34**, 555–566 (1995).

[9] I. Tropres, N. Pannetier, S. Grand, B. Lemasson, A. Moisan, M. Peoch, C. Remy, and E. L. Barbier, "Imaging the microvessel caliber and density: Principles and applications of microvascular MRI," Magnetic Resonance in Medicine **73**, 325–341 (2014).

[10] D. A. Yablonskiy and E. M. Haacke, "Theory of NMR signal behavior in magnetically inhomogeneous tissues: The static dephasing regime," Magnetic Resonance in Medicine **32**, 749–763 (1994).

[11] R.B.Buxton, ed., *Introduction to Functional Magnetic Resonance Imaging: Principles and Techniques* (Cambridge University Press, 2009).

[12] E. L. J. J. B. J.T. Bushberg, J.A. Seibert, ed., *The essential Physics of Medical Imaging* (Lippincott Williams and Wilkins, 2002).

[13] O. Bieri and K. Scheffler, "Effect of diffusion in inhomogeneous magnetic fields on balanced steady-state free precession," NMR in Biomedicine **20**, 1–10 (2007).

[14] N. Bloembergen, E. M. Purcell, and R. V. Pound, "Relaxation effects in nuclear magnetic resonance absorption," Physical Review **73**, 679–712 (1948).

[15] K. Uludağ, B. Müller-Bierl, and K. Uğurbil, "An integrative model for neuronal activity-induced signal changes for gradient and spin echo functional imaging," NeuroImage **48**, 150–165 (2009).

[16] K. Uludag, K. Ugurbil, and L. Berliner, eds., *fMRI: From Nuclear Spins to Brain Functions* (Springer US, 2015).

[17] T. SCIENTIFIC, "9000 Series Glass Particle Standards," `https://www.thermofisher.com/order/catalog/product/9120?SID=srch-srp-9120` (2008), [Online; accessed 18-December-2019].

[18] B. C. L. Sciences, "CC Standard Polystyrene Latex," `https://www.beckman.com/` (2008), [Online; accessed 18-December-2019].

[19] S. ha Hwang and S.-K. Lee, "Efficient experimental design for measuring magnetic susceptibility of arbitrarily shaped materials by MRI," Investigative Magnetic Resonance Imaging **22**, 141 (2018).

[20] J. L. Boxerman, P. A. Bandettini, K. K. Kwong, J. R. Baker, T. L. Davis, B. R. Rosen, and R. M. Weisskoff, "The intravascular contribution to fmri signal change: monte carlo modeling and diffusion-weighted studiesin vivo," Magnetic Resonance in Medicine **34**, 4–10 (1995).

Appendices

A. PHANTOM RELATED PICTURES

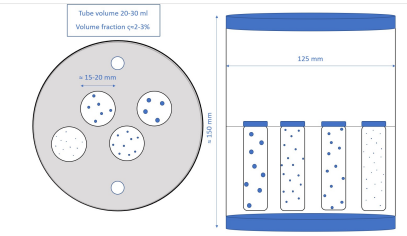

(a) sectional representation

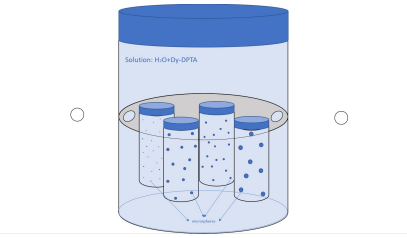

(b) Volume representation

Figure 37: First idea of design for the phantom.

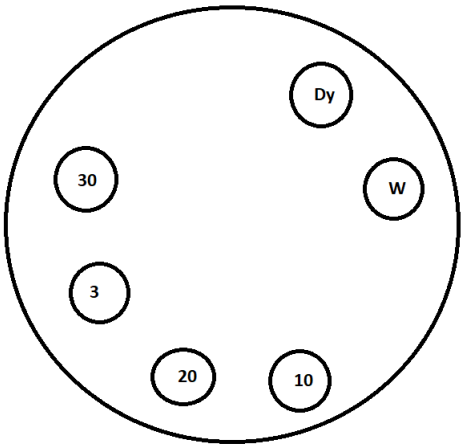

Figure 39: Qualitative distribution of the sample tubes in the images of experiment 2.

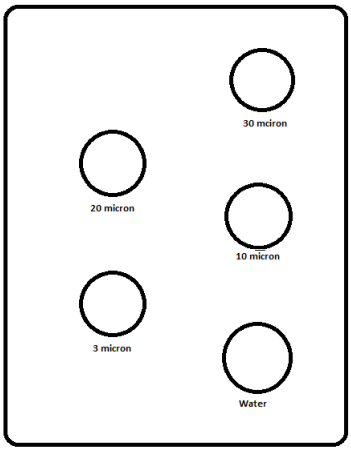

Figure 40: Qualitative distribution of the sample tubes in the images of experiment 4.

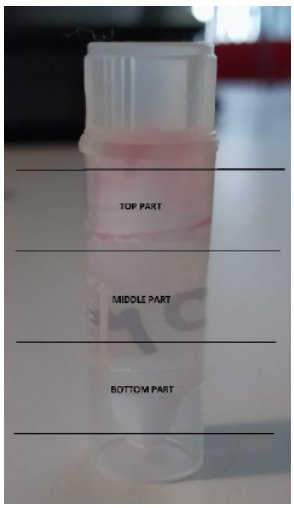

Figure 38: Qualitative partition structure of the sample tubes.

B. MULTI GRADIENT-ECHO SEQUENCE SPECIFICATIONS

The scanner used is a 7T MRI Philips scan. The steps followed in each scan are:

a) B_0 map+ shimming. Scan parameters are:

1. Data dimension was [64,64,30] for Experiments 2 and 3, and [64,64,35] for Experiment 4.
2. Spatial resolution: $\Delta x = \Delta y = \Delta z =$ 3.75mm.
3. Field of View (FOV) was [240,112.5,180] mm for Experiments 2 and 3, and [240,131.250,180] mm for Experiment 4.FOV=[AP,FH,RL] (anterior-posterior, feet-head ,right-left).
4. The echo time was TE=1.55ms.

5. The repetition time was TR=3.88ms for Experiments 2 and 3, and TR=3.88ms for Experiment 4. The shimming was performed to improve the B_0 homogeneity. Example can be seen in Fig 41.

b) B_1 map.

c) Multi Gradient-echo sequence. General parameters:

1. Data dimension [x,y,z,echo].

2. Flip angle of 90 degrees.

3. TR=5148.02 msec for Experiments 2 and 3, and TR=3542,536 msec for Experiment 4.

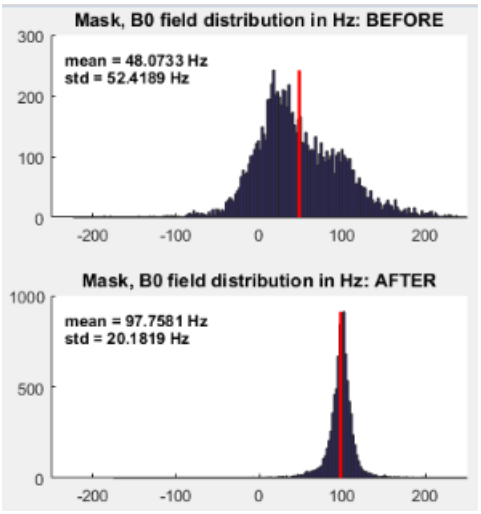

Figure 41: B_0 field distribution before and after the shimming.

C. THEORETICAL CALCULATION OF MAGNETIC SUSCEPTIBILITY AND RELAXATION RATES VALUES AT A CONSTANT VOLUME FRACTION.

The magnetic susceptibility of a mixture follows the Wiedemann's rule as

$$\chi = 4\pi \sum_{i=1}^{N} [c_i] \cdot \chi_{M_i} \tag{23}$$

where i represents the different components of the mixture, $[c_i]$ is the concentration of the component in mM and χ_{M_i} is the molar susceptibility of the i component. For a Dy-DTPA concentration of 5mM, the magnetic susceptibility of the solution is:

$$\chi_{sol} = \frac{-9.060}{4\pi} + \frac{2.953}{4\pi} = -0.486\text{ppm} \tag{24}$$

Table VI: Theoretical values of ΔR_2^* at $B_0 = 7$T, $\Delta\chi = 0.586$ppm. The values are calculated using the volume fractions of Experiment 3 and 4.

Diameter (μm)	ϱ(%)	ΔR_2^* (1/s)
3	0.0004	0.41
10	0.0056	4.98
20	0.0286	25.37
30	0.0285	25.34

According to Bieri et al. [13] the magnetic susceptibility of the polystyrene microspheres is 0.1 ppm. So, difference in χ due to the presence of microspheres is given by equation (25).

$$\Delta\chi = \chi_{objects} - \chi_{medium} = 0.1 - (-0.486) = 0.586\text{ppm} \tag{25}$$

Now, Yablonskiy et al.[10] obtained a theoretical relation of $\Delta R_2* = R_2*_{sphere} - R_2*_{sol}$ (Eq26) depending on the volume fraction of spheres (ϱ) and the difference in magnetic susceptibility ($\Delta\chi$).

$$\Delta R_2^* = \frac{2\pi}{3\sqrt{3}} \cdot \varrho \cdot \delta\omega_s = \frac{8\pi^2}{9\sqrt{3}} \cdot \varrho \cdot \gamma \cdot \Delta\chi \cdot B_0 \tag{26}$$

where $\delta\omega_s$ is explained in SectionII D.

Then, at $B_0 = 7$T, the theoretical values are shown in TableVI.

D. VOLUME FRACTION CALCULATION OF THE SAMPLE TUBES

To clarify, the volume fraction for each sample tube was calculated as

$$\varrho = \frac{V_{spheres}}{V_{tube}} \cdot 100 \tag{27}$$

where $V_{spheres}$ is the volume of spheres inside the sample tube in mL and $V_{tube} = 1.78$ mL is the volume of the sample tube itself. Then,

$$V_s = \frac{4\pi}{3} \cdot r^3 \cdot 10^6[\text{mL}] \tag{28}$$

where r is the radius of the sphere.
From [18], the particles/mL (ρ) that contain the Polystyrene microspheres bottles can be extracted. Then, if x mL are extracted from the bottle, the volume of spheres in the sample tube is:

$$V_{spheres} = V_s \cdot \rho \cdot x \tag{29}$$

Finally,

$$\varrho = \frac{V_s \cdot \rho \cdot x}{1.78} \cdot 100 \tag{30}$$